EES Batteries

ROYAL SOCIETY OF CHEMISTRY

PAPER

View Article Online
View Journal | View Issue

Cite this: *EES Batteries*, 2025, **1**, 495

A high Al-doping ratio halide solid electrolyte with a 3D Li-ion transport framework†

Yi-Xuan Li,‡ Li-Ping Cui,‡ Shu Zhang, ‡ Peng-Fei Sun, Cheng-Dong Fang, Yu-Hang Zhang, Liu-Bin Feng and Jia-Jia Chen *

Received 10th November 2024,
Accepted 13th March 2025

DOI: 10.1039/d4eb00030g

rsc.li/EESBatteries

Rare earth metal-based halide solid electrolytes (HSEs) are among the most promising electrolyte candidates for novel solid-state batteries. However, reducing the content of rare earth metals while still retaining high Li-ion conductivity remains a great challenge. In this work, we report a class of Al-substituted halide solid electrolytes, $Li_3Al_xY_{1-x}Cl_6$, and explore the impact of Al substitution content on the halide structure and lithium-ion transport. Interestingly, $Li_3Al_{0.7}Y_{0.3}Cl_6$ exhibits a high ionic conductivity of 1.05×10^{-4} S cm^{-1} with a high Al substitution ratio of 70% even at 25 °C. Bond valence site energy (BVSE) analysis reveals that the disorderly substitution of a higher proportion of smaller atomic radius Al elements into the structure potentially opens 3D migration pathways and reduces the energy barrier for lithium ion migration, thereby enhancing Li ion conductivity. As a result, the as-prepared $Li_3Al_xY_{1-x}Cl_6$ demonstrated a stable operation of Li electrochemical stripping and plating at 100 μA cm^{-2} over 2500 h.

Broader context

Solid-state batteries, which utilize solid electrolytes instead of traditional liquid electrolytes, significantly enhance battery safety and stability. As a core component of solid-state batteries, the properties of the solid electrolyte directly determine the overall performance of the battery. Rare earth metal-based halide solid electrolytes (HSEs) are among the most promising electrolyte candidates for novel solid-state batteries. However, reducing the content of rare earth metals while retaining high Li-ion conductivity and anode interface stability remains key to driving their widespread application. The preparation of substituted HSEs using aluminum, an element with high abundance, can significantly reduce production costs. Aluminum doping modifies the crystal structure of the electrolyte, thereby influencing its electrochemical performance. Both theoretical calculations and experimental results indicate that the disorderly substitution of smaller-radius aluminum atoms in higher proportions may open three-dimensional migration channels, reducing the energy barrier for lithium-ion migration and thereby enhancing lithium-ion conductivity. This approach offers a new strategy for designing stable, low-cost halide solid electrolytes.

Introduction

All-solid-state batteries (ASSB) have the advantages of higher safety and energy density, longer life and better design flexibility compared with traditional lithium batteries with liquid organic electrolytes.[1] Solid-state electrolytes (SSEs) play a crucial role in the overall performance of all-solid-state batteries.[2–4] Current research focuses on exploring various solid electrolyte materials, including oxides ($Li_7La_3Zr_2O_{12}$, $Li_{1.5}Al_{0.5}Ge_{1.5}(PO_4)_3$, and $La_{0.56}Li_{0.33}TiO_3$), sulfides ($Li_{10}GeP_2S_{12}$, Li_6PS_5Cl, and $Li_7SnP_2S_{12}$), and organic polymers (polyethylene oxide and polyvinylidene fluoride).[5–11] Recently, emerging halide solid electrolytes have garnered significant research interest. Most of the halide solid electrolytes based on rare earth elements exhibit high ionic conductivity, broad electrochemical stability windows and notable flexibility.[12,13] However, the high costs, along with the interfacial side reactions occurring between these materials and lithium metal anodes, have constrained the development of this category of SSEs.[14–18]

Janek *et al.* first found that halides Li_3InCl_6 and Li_3YCl_6 further react with metallic Li, undergoing decomposition into LiCl and the corresponding rare earth metals, ultimately leading to the collapse of the SSE structure.[19] Thus, several strategies based on *in situ*/*ex situ* interfacial layer modifications have been proposed to stabilize the operation of halide solid-state batteries. For instance, Asano *et al.* first utilized a Li–In

State Key Laboratory for Physical Chemistry of Solid Surfaces, Innovation Laboratory for Sciences and Technologies of Energy Material of Fujian Province (IKKEM), Collaborative Innovation Center of Chemistry for Energy Materials (iChem), Engineering Research Center of Electrochemical Technologies of Ministry of Education, Department of Chemistry, College of Chemistry and Chemical Engineering, Xiamen University, Xiamen, Fujian, 361005, China.
E-mail: JiaJia.Chen@xmu.edu.cn

†Electronic supplementary information (ESI) available: Synthetic procedures, materials characterisation, crystal structure, electrochemical characterisation and DFT modelling data. See DOI: https://doi.org/10.1039/d4eb00030g

‡These authors contributed equally to this work.

alloy as an anode to mitigate reactions with the halides.[20] Sun *et al.* designed a Li_6PS_5Cl transition layer between the halide and lithium metal, creating a continuous lithium ion pathway through the sulfide interfacial reaction, enabling the assembled lithium symmetric cell to achieve a stable cycle life of over 500 hours.[21] In addition, Sun's team designed and developed a series of novel substituted mixed metal halides and thoroughly investigated their structural evolution among different types of halide solid state electrolytes.[22] On the other hand, to reduce the cost of solid electrolytes, Ma *et al.* have developed a non-rare earth halide, Li_2ZrCl_6, which achieves an ionic conductivity of 10^{-4} S cm^{-1} at room temperature. This substitution strategy provides a viable design pathway for lowering the cost of halide electrolytes.[23]

However, it is still a challenge to directly modify the structure of halide solid electrolytes to tune the pathways for lithium-ion transport, especially with the substitution of abundant elements. In this work, we first report a chloride-based inorganic solid electrolyte substituted with aluminium (Al), $Li_3Al_xY_{1-x}Cl_6$ ($0 \le x \le 1$), which exhibits an ionic conductivity of 1.05×10^{-4} S cm^{-1} under ambient conditions with a high Al substitution ratio of 70%. Theoretical calculations were employed to elucidate the influence of structural changes on the lithium-ion transport pathways. Moreover, the as-prepared $Li_3Al_xY_{1-x}Cl_6$ demonstrated a stable operation of Li electrochemical stripping and plating at 100 μA cm^{-2} for 2500 h.

Results and discussion

Structural characterization of the halide solid state electrolyte $Li_3Al_xY_{1-x}Cl_6$

Aluminum, a highly abundant metal element in the Earth's crust, is much cheaper than rare-earth halides (Fig. 1a). For instance, the cost of $AlCl_3$ is less than 20 USD per kg, which is only 2.7% of that of YCl_3 and 1.4% of that of $InCl_3$. Thus, the introduction of aluminum can significantly alleviate the cost issues associated with halide solid electrolytes.[24–26] Meanwhile, the use of aluminium helps to minimise reliance on scarce and expensive rare earth elements, making this type of solid-state electrolyte more viable for large-scale applications. To this end, halide solid electrolytes $Li_3Al_xY_{1-x}Cl_6$ (LAYC) with different Al^{3+}/Y^{3+} molar ratios are prepared using high-speed ball milling (Fig. S1†). The molded LAYC pellets are analyzed using scanning electron microscopy (SEM) and energy-dispersive spectroscopy (EDS) elemental mapping (Fig. 1b). The images showed that the LAYC surface was smooth, with uniform particle size and a homogeneous distribution of Y, Al, and Li elements.

To determine the crystal structure of the electrolytes, X-ray diffraction (XRD) analysis was performed on $Li_3Al_xY_{1-x}Cl_6$ electrolytes with different Al^{3+}/Y^{3+} contents (Fig. 2). The XRD diffraction patterns show that the characteristic peaks of $Li_3Al_xY_{1-x}Cl_6$ samples containing Al^{3+} substitutions are significantly different from those of Li_3YCl_6 and $LiAlCl_4$, indicating that the introduction of Al induces a transformation of the

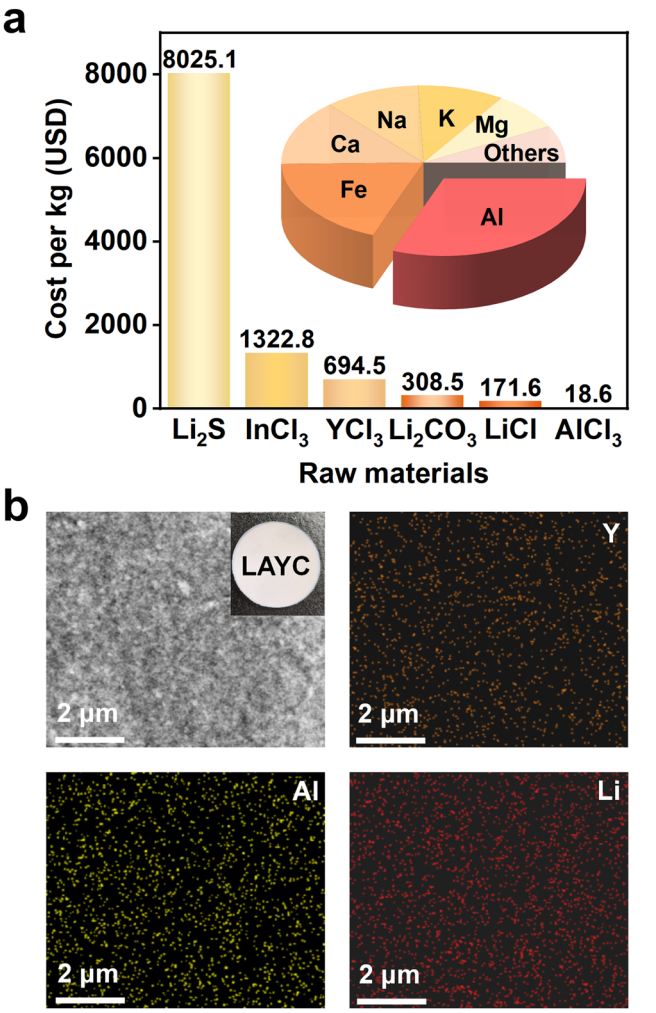

Fig. 1 (a) The cost of solid electrolyte raw materials and the abundance map of crustal metal elements. (b) SEM image and EDS elemental mapping of $Li_3Al_xY_{1-x}Cl_6$ for Y, Al, and Li.

lattice structure. The structural tuning resulting from adjusting the Al^{3+}/Y^{3+} ratio in $Li_3Al_xY_{1-x}Cl_6$ ($0 < x < 1$) is shown in Fig. S2a.† Li_3YCl_6 exhibits a trigonal system with the space group $P3m1$ and a densely packed hexagonal close-packed (hcp) arrangement of anions.[11,16] When substituted with Al, the XRD patterns of LAYC transform into the monoclinic system with the space group $C2/m$ (the previously reported Li_3InCl_6 standard pattern, ICSD no. 04-009-9027) and a cubic close-packed (ccp) arrangement of anions (Fig. S2b†).[27]

Commonly, the crystallographic structure of metal halide superionic conductors is characterized by the formula Li_3MX_6, where M denotes a trivalent rare earth metal and X represents a halogen. The doping of the M element within the lattice leads to vacancy creation, and the resultant structure is influenced by factors such as the ionic radii of cations and anions, the polarity, and the modes of ionic packing. Accordingly, based on the laws of ionic packing, the changes in the crystal structure upon the introduction of Al atoms can be explained by the ratio of the radii of cations to anions (Fig. 3a). The

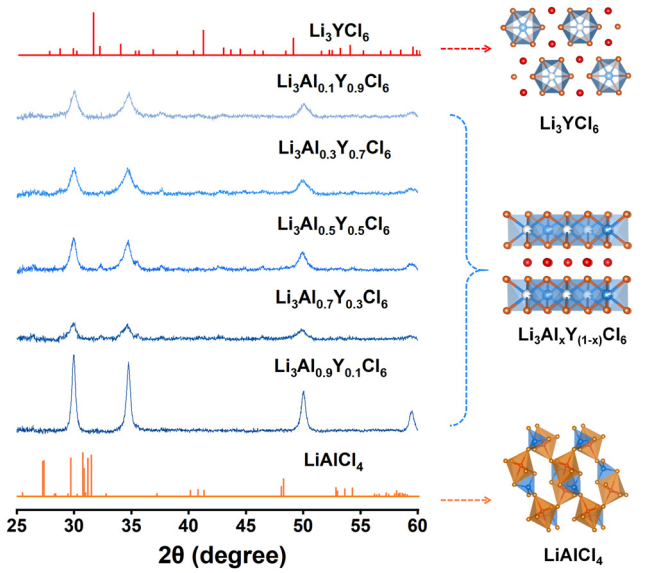

Fig. 2 XRD pattern characterization of LAYC electrolytes.

extrapolated results show that the doping of Al atoms adjusts the occupation of cations in Li_3YCl_6, which in turn changes the way the atoms stack in the structure. Even a high Al substitution of $Li_3Al_xY_{1-x}Cl_6$ does not exhibit a structural correlation with $LiAlCl_4$ in the $P2_1/c$ space group. This lattice structure transformation should be due to the influence of the ionic radius on the structural transition, which can be analyzed by using the "cation polarization factor" (Fig. 3b and Table S1†).[22] It is suggested that this crystal structure transition is regulated by the metal ionic radii (the average of the ionic radii of multiple metals present). The difference in atomic radii between the dopant and the atoms in the original material induces changes in lattice parameters, leading to lattice distortions and alterations in stacking density and arrangement.[28] Furthermore, variations in the electron cloud density between the dopant and the original material atoms affect the interatomic forces, lowering the kinetic barriers for structural transformation, thereby facilitating the transition of the crystal structure towards a thermodynamically stable state.[29] It has been shown that there is a complex correlation between the composition and structure of a material and that changes in this structure may also affect the electrochemical properties of the material.

Al doping ratio regulates the Li^+ migration barrier within $Li_3Al_xY_{1-x}Cl_6$

The ion conductivity and activation energy of LAYC solid electrolytes are also significantly influenced by the Al substitution content (Fig. 4 and S3†). Specifically, $Li_3Al_{0.7}Y_{0.3}Cl_6$ exhibited the highest ion conductivity of 1.05×10^{-4} S cm^{-1} at 25 °C, which is two orders of magnitude higher than that of $Li_3Al_{0.1}Y_{0.9}Cl_6$ (Fig. 4a). The activation energy of LAYC calculated using Arrhenius plots is in the range of 0.277 – 0.363 e V (Fig. 4b). Additionally, when Al^{3+}/Y^{3+} = 0.7, the electrolyte showed a relatively low activation energy of 0.303 eV. This is competitive with those of most of the reported halide and oxide solid electrolytes,[30] indicating the emergence of a low Li ion migration energy barrier. However, it is noteworthy that a higher Al substitution of $Li_3Al_{0.9}Y_{0.1}Cl_6$ exhibited a decreased ion conductivity compared to $Li_3Al_{0.7}Y_{0.3}Cl_6$. This is reasonable, as a high Al content will brings the structure close to $LiAlCl_4$, which exhibits a low Li-ion conductivity of 1.2×10^{-6} at room temperature.[31]

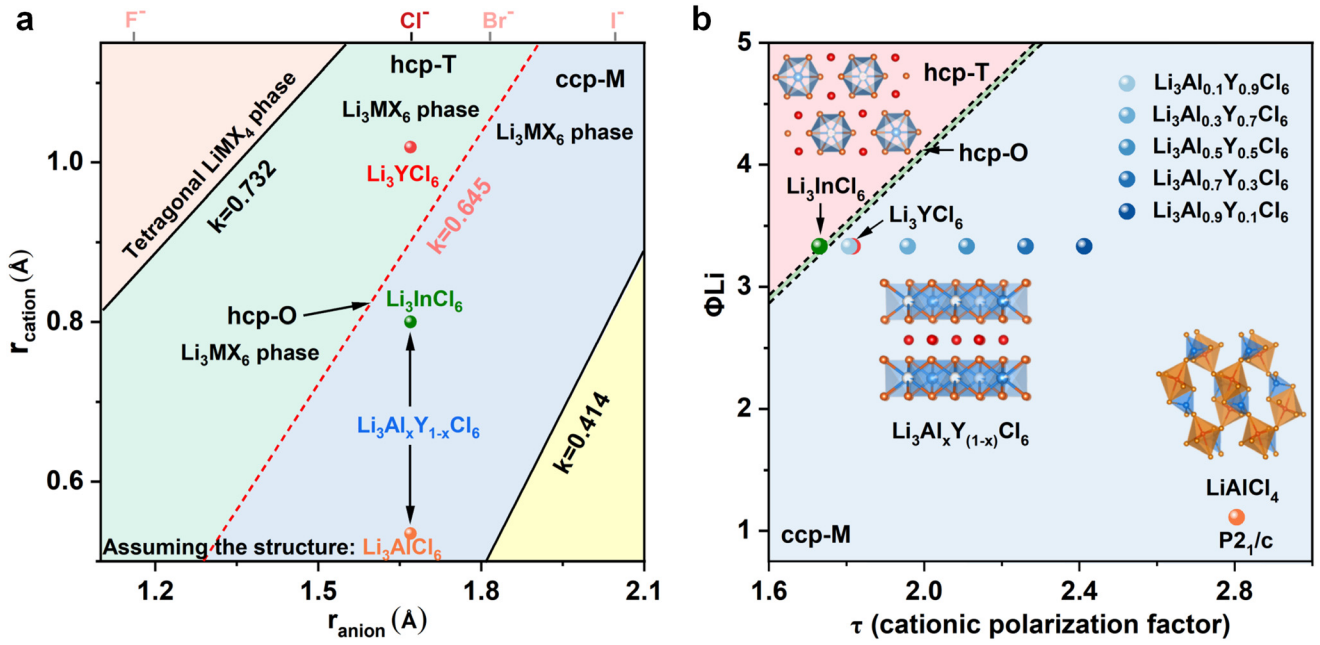

Fig. 3 (a) Ionic radius rule of representative hcp-T and ccp-M type Li_aMX_b halides. (b) Cationic polarization factor of LAYC electrolytes.

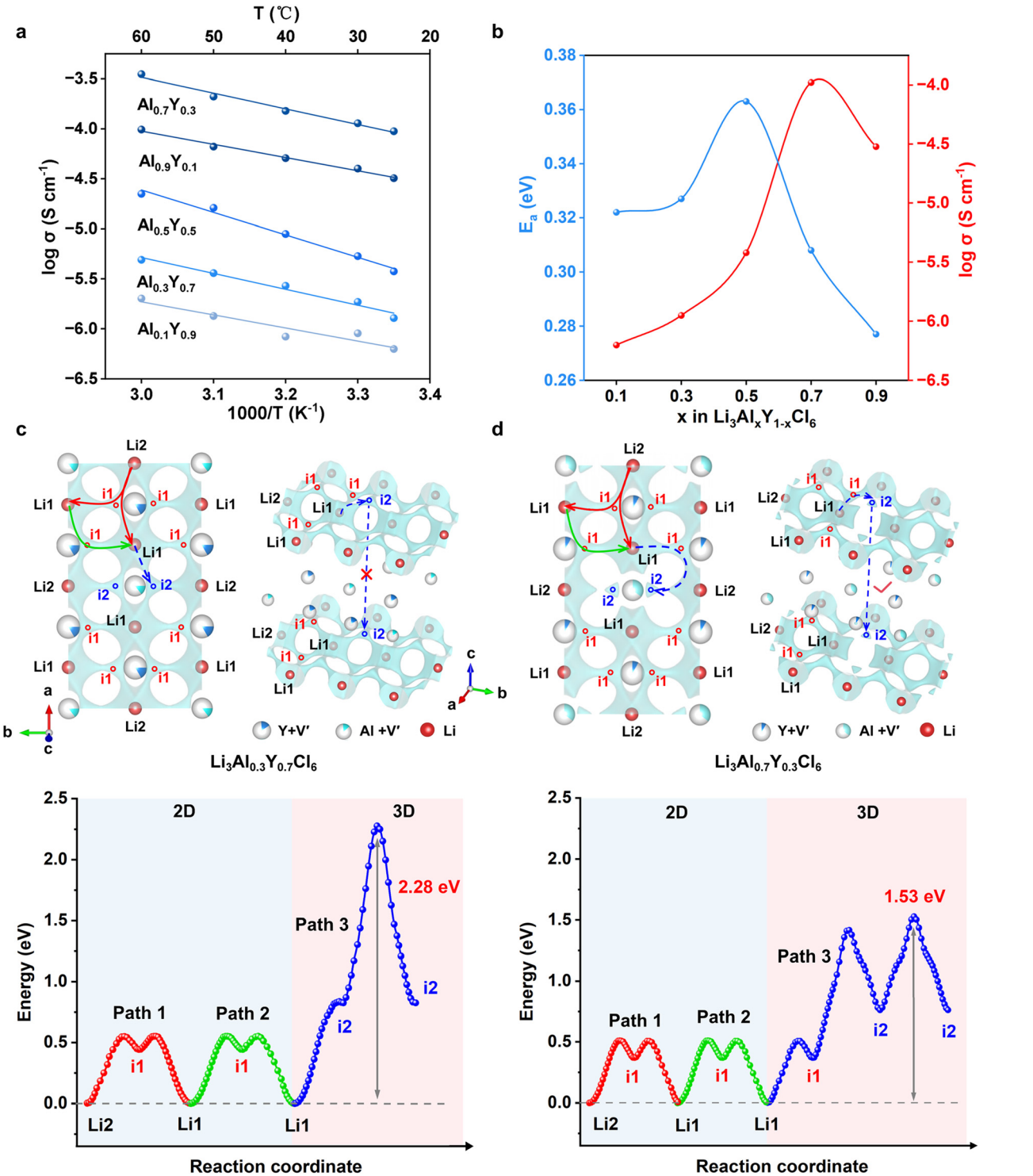

Fig. 4 (a) Arrhenius plots of LAYC and (b) plots of ionic conductivity at 25 °C and activation energy of LAYC. BVSE theoretical calculation of lithium-ion transport *via* two- and three-dimensional migration pathways and the related migration energy barrier in (c) $Li_3Al_{0.3}Y_{0.7}Cl_6$ and (d) $Li_3Al_{0.7}Y_{0.3}Cl_6$.

Based on structural analysis, there are two migration directions for Li ions in $Li_3Al_xY_{1-x}Cl_6$: two-dimensional (2D) migration along the *a*–*b* plane and three-dimensional (3D) migration between *a*–*b* planes (Fig. 4c and d). The sites of Li, Al^{3+}/Y^{3+}, and vacancies are in a ratio of 3 : 1 : 2 within this distorted rock-salt structure (Fig. S4–7†). These inherent vacancies in principle contribute to the ion conductivity of the solid electrolyte *via* 3D migration between *a*–*b* planes.[32,33] As illustrated in Fig. 4c and d, BVSE calculations reveal that Li2–i1–Li1 and Li1–i1–Li1 (Paths 1 and 2) within the *a*–*b* plane are the most favourable 2D migration

pathways. Intermediate 1 (i1), located directly beneath the Y atom, serves as a necessary intermediate site for Li ions migrating between Li2 and Li1 sites. BVSE results indicate that the migration energy barrier for Li ions along the *a*–*b* plane is slightly higher in $Li_3Al_{0.3}Y_{0.7}Cl_6$ compared to that in $Li_3Al_{0.7}Y_{0.3}Cl_6$. This is attributed to the larger atomic radius of Y, which inhibits the transport of Li ions to the i1 site. Indeed, a higher content of Y^{3+} will affect the migration of Li ions between Li2 and Li1 sites.

The 3D migration of Li ions between the *a*–*b* planes requires the intermediate 2 (i2) site, located directly beneath the Al atom, forming an effective 3D network through i2–i2 chain migration (Path 3). To achieve this, Li ions in $Li_3Al_xY_{1-x}Cl_6$ must first reach the i2 site. In $Li_3Al_{0.3}Y_{0.7}Cl_6$, Li ions directly migrate from the Li1 site to the i2 site (Path 3 in Fig. 4c). In contrast, $Li_3Al_{0.7}Y_{0.3}Cl_6$ requires a slightly higher energy barrier for migration from the Li1 site through the i1 site to the i2 site (Path 3 in Fig. 4d). This is attributed to a higher Al content, which increases spatial hindrance for Li ions migrating to the i2 site within the *a*–*b* plane. However, this also increases the likelihood of vacancy formation around the Al sites in the Al^{3+}/Y^{3+} atomic layer, significantly reducing

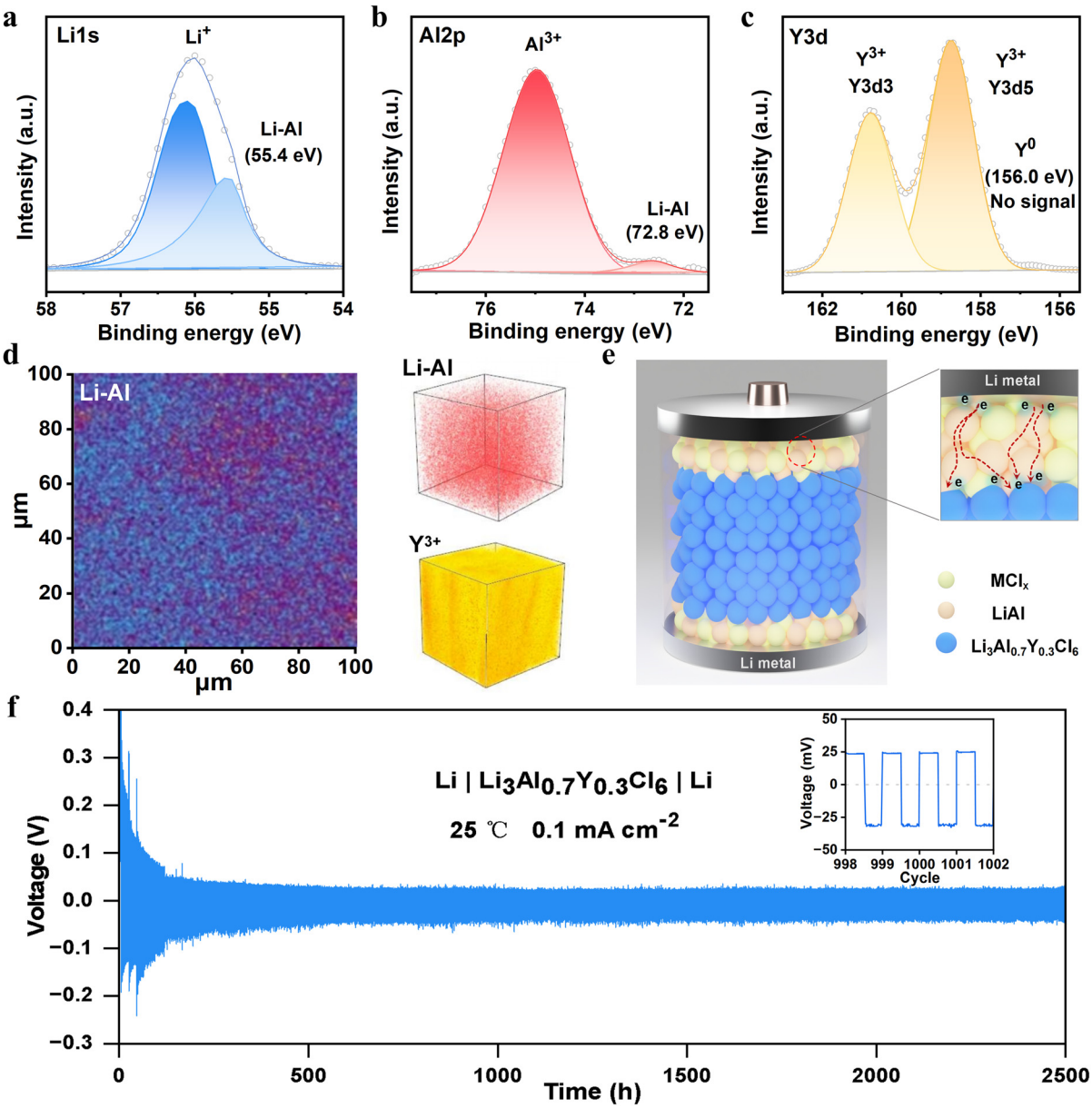

Fig. 5 XPS spectra of (a) Li 1s, (b) Al 2p and (c) Y 3d in the interfacial reaction layer. (d) 2D diagram and 3D distribution of Li–Al alloy in the interfacial reaction layer obtained by TOF-SIMS. (e) Scheme of the interfacial reaction mechanism of the Li|$Li_3Al_{0.7}Y_{0.3}Cl_6$|Li symmetric battery. (f) The electrochemical Li stripping and plating investigations of the Li|$Li_3Al_{0.7}Y_{0.3}Cl_6$|Li symmetric cell with a current density of 0.1 mA cm^{-2} at 25 °C (the inset shows stripping and plating curves from 998 to 1002 cycles).

the 3D migration barrier to 1.53 eV (Path 3 in Fig. 4d), compared to 2.28 eV for $Li_3Al_{0.3}Y_{0.7}Cl_6$ (Path 3 in Fig. 4c). Moreover, it is noteworthy that excessively high aluminium doping is not conducive to improving conductivity. In $Li_3Al_{0.9}Y_{0.1}Cl_6$, a significant decline in conductivity was observed, which can be attributed to the oversaturation of Al doping, leading to the change of the chemical composition and crystal orientation within the material. This results in the presence of a large amount of excess LiCl phase. This observation aligns with the sharp increase in XRD peak intensity for the $Li_3Al_{0.9}Y_{0.1}Cl_6$ material in Fig. 2. As a result, the substitution of Al at an appropriate ratio could potentially open 3D migration pathways for lithium ions, thereby enhancing ion conductivity.

Interfacial stability assessment of $Li|Li_3Al_{0.7}Y_{0.3}Cl_6|Li$ symmetric batteries

As we have known, halide electrolytes have poor compatibility with metallic Li, because of their high chemical reactivity, intense interfacial reactions, and poor electrolyte stability.[34] The interface stability of $Li_3Al_{0.7}Y_{0.3}Cl_6$ with metallic Li during electrochemical stripping and plating was further studied in detail. X-ray photoelectron spectroscopy (XPS) characterization of the interface after cycling was performed. The Li 1s spectrum shows prominent characteristic peaks of the Li–Al alloy (55.4 eV) and Li^+ in LAYC (Fig. 5a). The Al 2p spectrum also exhibits significant characteristic peaks of the Li–Al alloy (72.8 eV), along with characteristic peaks attributed to Al^{3+} in LAYC (Fig. 5b). Additionally, the Y 3d spectrum displays characteristic peaks attributed to Y^{3+} in LAYC, while no characteristic peak is detected at the position of the Y^0 signal (156.0 eV), indicating that Y^{3+} has not been reduced (Fig. 5c). In contrast, when Li_3YCl_6 is used as the electrolyte, Y^{3+} is usually reduced to Y^0 upon interfacial reaction with lithium.[20,35,36] Furthermore, combining the time-of-flight secondary ion mass spectrometry (TOF-SIMS) analysis of the battery interfacial reaction materials (Fig. 5d and Fig. S8†), a uniform distribution of the Li–Al alloy in the interfacial reaction layer can be clearly observed. This fact indicates that the Al substitution strategy significantly influences interfacial reactions with the formation of the Li–Al alloy from Al^{3+} in LAYC.

As illustrated in Fig. 5e and S9,† a portion of the Al in the $Li_3Al_{0.7}Y_{0.3}Cl_6$ electrolyte participates in the formation of the Li–Al alloy, and a small amount of mixed metal chloride MCl_x is produced at the interface. It seems that this interface layer effectively slows down reactions between rare-earth elements and lithium metal. Long-term electrochemical cycling stability between lithium metal and LAYC with different Al^{3+}/Y^{3+} ratios was also investigated. Both Li_3YCl_6 and $Li_3Al_{0.3}Y_{0.7}Cl_6$ show a large and increasing Li electrochemical stripping and plating overpotential even at a high operating temperature of 60 °C and a low current density of 0.03 mA cm^{-2}, while $Li_3Al_{0.7}Y_{0.3}Cl_6$ shows a decreasing trend in overpotential (Fig. S10†). Further *in situ* AC impedance testing confirmed that stable interfacial stability can be achieved within 30 cycles of the $Li|Li_3Al_{0.7}Y_{0.3}Cl_6|Li$ symmetric cell (Fig. S11†), indicating the formation of a stable SEI layer at the interface. As a result, the assembled $Li|Li_3Al_{0.7}Y_{0.3}Cl_6|Li$ cell can achieve stable cycling performance over 2500 hours at 25 °C under 0.1 mA cm^{-2}, with a small overpotential of less than 50 mV in long-term testing (Fig. 5f).

Conclusions

In summary, we have successfully designed a series of $Li_3Al_xY_{1-x}Cl_6$ halide solid electrolytes and found that aluminum substitution notably transforms the crystal structure of the halides from an hcp to a ccp structure. This transition alters the occupancy of the metal elements and vacancies, significantly impacting the corresponding ionic conductivity and electrochemical performance. According to BVSE calculations, the lithium-ion transport pathways are also changed by the substitution ratio of Al. An appropriate substitution ratio of Al will lead to a lower lithium-ion migration barrier, thus enhancing interfacial ion transport. At 25 °C, a symmetric lithium cell incorporating $Li_3Al_{0.7}Y_{0.3}Cl_6$ demonstrated stable cycling performance over 2500 h. Furthermore, with an Al content as high as 0.7, the reduced rare-earth element content could decrease the cost of the halide by more than 40%. This study presents a structure- and mechanism-oriented approach for designing stable, low-cost halide solid-state electrolytes with high compatibility with metallic Li.

Author contributions

J. C. proposed the project. Y. L., L. C. and S. Z. wrote this manuscript. Y. L. planned and performed the experiments. L. C. performed the structural analysis. S. Z. performed the BVSE calculations. L. F. assisted in spectroscopic tests. P. S., C. F. and Y. Z. assisted in performing the electrochemical measurements. Y. L., L. C. and S. Z. contributed equally to this work.

Data availability

The data supporting this article have been included as part of the ESI.† Additionally, the original experimental data can be accessed from the corresponding author to ensure transparency and support further research endeavors.

Conflicts of interest

The authors declare no conflict of interest.

Acknowledgements

We acknowledge financial support from the National Natural Science Foundation of China (NSFC, 22393901, 22021001, 22272143, and 22441030), the National Key Research and

Development Program (2021YFA1502300), the Fundamental Research Funds for the Central Universities (20720220009), the Natural Science Foundation of Fujian Province (2024J01213135) and the Innovation Laboratory for Sciences and Technologies of Energy Materials of Fujian Province (IKKEM, RD2023020801).

References

1 K. Y. Tuo, C. W. Sun and S. Q. Liu, *Electrochem. Energy Rev.*, 2023, **6**, 17.
2 J. Janek and W. G. Zeier, *Nat. Energy*, 2023, **8**, 230–240.
3 J. Wen, Y. Huang, J. Duan, Y. Wu, W. Luo, L. Zhou, C. Hu, L. Huang, X. Zheng, W. Yang, Z. Wen and Y. Huang, *ACS Nano*, 2019, **13**, 14549–14556.
4 J. J. Li, H. L. Wei, Y. Peng, L. F. Geng, L. M. Zhu, X. Y. Cao, C. S. Liu and H. Pang, *Chem. Commun.*, 2019, **55**, 7922–7925.
5 J. van den Broek, S. Afyon and J. L. M. Rupp, *Adv. Energy Mater.*, 2016, **6**, 1600736.
6 F. P. Zhao, J. W. Liang, C. Yu, Q. Sun, X. N. Li, K. Adair, C. H. Wang, Y. Zhao, S. M. Zhang, W. H. Li, S. X. Deng, R. Y. Li, Y. N. Huang, H. Huang, L. Zhang, S. Q. Zhao, S. G. Lu and X. L. Sun, *Adv. Energy Mater.*, 2020, **10**, 1903422.
7 D. E. Fenton, J. M. Parker and P. V. Wright, *Polymer*, 1973, **14**, 589.
8 X. K. Liu, Y. X. Zhou, F. H. Mi, X. L. Ma and C. W. Sun, *Energy Storage Mater.*, 2024, **72**, 103737.
9 K. Y. Tuo, C. W. Sun, C. A. Lopez, M. T. Fernandez-Dıaz and J. A. Alonso, *J. Mater. Chem. A*, 2023, **11**, 15651–15662.
10 K. Y. Tuo, F. S. Yin and C. W. Sun, *ACS Sustainable Chem. Eng.*, 2024, **12**, 7012–7025.
11 K. Y. Tuo, F. S. Yin, F. H. Mi and C. W. Sun, *J. Energy Chem.*, 2023, **87**, 12–23.
12 H. X. Mei, P. Piccardo, A. Cingolani and R. Spotorno, *J. Power Sources*, 2023, **553**, 232257.
13 C. H. Wang, J. W. Liang, J. T. Kim and X. L. Sun, *Sci. Adv.*, 2022, **8**, eadc9516.
14 W. X. Ji, D. Zheng, X. X. Zhang, T. Y. Ding and D. Y. Qu, *J. Mater. Chem. A*, 2021, **9**, 15012–15018.
15 J. Luo, Q. Sun, J. Liang, K. Adair, F. Zhao, S. Deng, Y. Zhao, R. Li, H. Huang, R. Yang, S. Zhao, J. Wang and X. Sun, *ACS Energy Lett.*, 2023, **8**, 3676–3684.
16 H. Kwak, D. Han, J. Lyoo, J. Park, S. H. Jung, Y. Han, G. Kwon, H. Kim, S. T. Hong, K. W. Nam and Y. S. Jung, *Adv. Energy Mater.*, 2021, **11**, 2003190.
17 H. Kwak, D. Han, J. P. Son, J. S. Kim, J. Park, K.-W. Nam, H. Kim and Y. S. Jung, *Chem. Eng. J.*, 2022, **437**, 135413.
18 K. Wang, Q. Y. Ren, Z. Q. Gu, C. M. Duan, J. Z. Wang, F. Zhu, Y. Y. Fu, J. P. Hao, J. F. Zhu, L. H. He, C. W. Wang, Y. Y. Lu, J. Ma and C. Ma, *Nat. Commun.*, 2021, **12**, 4410.
19 L. M. Riegger, R. Schlem, J. Sann, W. G. Zeier and J. Janek, *Angew. Chem., Int. Ed.*, 2021, **60**, 6718–6723.
20 T. Asano, A. Sakai, S. Ouchi, M. Sakaida, A. Miyazaki and S. Hasegawa, *Adv. Mater.*, 2018, **30**, 1803075.
21 C. H. Wang, J. W. Liang, J. Luo, J. Liu, X. N. Li, F. P. Zhao, R. Y. Li, H. Huang, S. Q. Zhao, L. Zhang, J. T. Wang and X. L. Sun, *Sci. Adv.*, 2021, **7**, eabh1896.
22 X. N. Li, J. T. Kim, J. Luo, C. T. Zhao, Y. Xu, T. Mei, R. Y. Li, J. W. Liang and X. L. Sun, *Nat. Commun.*, 2024, **15**, 53.
23 L. Zhou, T. Zuo, C. Li, Q. Zhang, J. Janek and L. F. Nazar, *ACS Energy Lett.*, 2023, **8**, 3102–3111.
24 M. Wang, F. Zhang, C. S. Lee and Y. B. Tang, *Adv. Energy Mater.*, 2017, **7**, 1700536.
25 Y. L. Liang, H. Dong, D. Aurbach and Y. Yao, *Nat. Energy*, 2020, **5**, 646–656.
26 S. Yu, J. Noh, B. Kim, J. H. Song, K. Oh, J. Yoo, S. Lee, S. O. Park, W. Kim, B. Kang, D. Kil and K. Kang, *Science*, 2023, **382**, 573–579.
27 X. N. Li, J. W. Liang, J. Luo, M. N. Banis, C. H. Wang, W. H. Li, S. X. Deng, C. Yu, F. P. Zhao, Y. F. Hu, T. K. Sham, L. Zhang, S. Q. Zhao, S. G. Lu, H. Huang, R. Y. Li, K. R. Adair and X. L. Sun, *Energy Environ. Sci.*, 2019, **12**, 2665–2671.
28 J. Park, D. Han, H. Kwak, Y. Han, Y. J. Choi, K.-W. Nam and Y. S. Jung, *Chem. Eng. J.*, 2021, **425**, 130630.
29 D. Park, H. Park, Y. Lee, S.-O. Kim, H.-G. Jung, K. Y. Chung, J. H. Shim and S. Yu, *ACS Appl. Mater. Interfaces*, 2020, **12**, 34806–34814.
30 Y. C. Yin, J. T. Yang, J. D. Luo, G. X. Lu, Z. Huang, J. P. Wang, P. Li, F. Li, Y. C. Wu, T. Tian, Y. F. Meng, H. S. Mo, Y. H. Song, J. N. Yang, L. Z. Feng, T. Ma, W. Wen, K. Gong, L. J. Wang, H. X. Ju, Y. G. Xiao, Z. Y. Li, X. Y. Tao and H. B. Yao, *Nature*, 2023, **616**, 77–83.
31 N. Tanibata, S. Takimoto, K. Nakano, H. Takeda, M. Nakayama and H. Sumi, *ACS Mater. Lett.*, 2020, **2**, 880–886.
32 K. Wang, Z. Gu, Z. Xi, L. Hu and C. Ma, *Nat. Commun.*, 2023, **14**, 1396.
33 X. N. Li, J. W. Liang, N. Chen, J. Luo, K. R. Adair, C. H. Wang, M. N. Banis, T. K. Sham, L. Zhang, S. Q. Zhao, S. G. Lu, H. Huang, R. Y. Li and X. L. Sun, *Angew. Chem., Int. Ed.*, 2019, **58**, 16427–16432.
34 W. Xu, J. L. Wang, F. Ding, X. L. Chen, E. Nasybutin, Y. H. Zhang and J. G. Zhang, *Energy Environ. Sci.*, 2014, **7**, 513–537.
35 H. Duan, C. H. Wang, R. Z. Yu, W. H. Li, J. M. Fu, X. F. Yang, X. T. Lin, M. T. Zheng, X. A. Li, S. X. Deng, X. G. Hao, R. Y. Li, J. T. Wang, H. Huang and X. L. Sun, *Adv. Energy Mater.*, 2023, **13**, 2300815.
36 T. Dai, S. Y. Wu, Y. X. Lu, Y. Yang, Y. Liu, C. Chang, X. H. Rong, R. J. Xiao, J. M. Zhao, Y. H. Liu, W. H. Wang, L. Q. Chen and Y. S. Hu, *Nat. Energy*, 2023, **8**, 1221–1228.